energies

MDPI

Article

Smart Switching in Single-Phase Grid-Connected Photovoltaic Power Systems for Inrush Current Elimination

Gerardo de J. Martínez-Figueroa, Santiago Bogarra and Felipe Córcoles *

Department of Electrical Engineering, ESEIAAT, Universitat Politècnica de Catalunya, 08222 Terrassa, Spain; gerardo.de.jesus.martinez@upc.edu (G.d.J.M.-F.); santiago.bogarra@upc.edu (S.B.)
* Correspondence: felipe.corcoles@upc.edu

Abstract: Grid-connected photovoltaic (PV) power systems are one of the most promising technologies to address growing energy demand and ecological challenges. This paper proposes smart switching to mitigate inrush currents during the connection of single-phase transformers used in PV systems. An effective inrush current mitigation contributes to the reliability of PV systems. The inrush current severity is influenced by the pseudorandom residual flux at the transformer core and the energization point-on-wave. The most common approach to avoid inrush currents is controlled connection, which requires prior knowledge of the residual flux. However, the residual flux can differ in each case, and its measurement or estimation can be impractical. The proposed smart switching is based on a comprehensive analysis of the residual flux and the de-energization trajectories, and only requires two pieces of data (ϕ_{RM} and ϕ_0, flux values of the static and dynamic loops when the respective currents are null), calculated from two simple no-load tests. It has a clear advantage over common approaches: no need to estimate or measure the residual flux before each connection, avoiding the need for expensive equipment or complex setups. Smart switching can be easily implemented in practical settings, as it considers different circuit breakers with distinctive aperture features, making it cost-effective for PV systems.

Keywords: photovoltaic; single-phase transformer; inrush current; residual flux; hysteresis

check for updates

Citation: Martínez-Figueroa, G.d.J.; Bogarra, S.; Córcoles, F. Smart Switching in Single-Phase Grid-Connected Photovoltaic Power Systems for Inrush Current Elimination. *Energies* **2023**, *16*, 7211. https://doi.org/10.3390/en16207211

Academic Editors: Omar Ali Beg, Zongjie Wang and Shan Zuo

Received: 15 September 2023
Revised: 17 October 2023
Accepted: 22 October 2023
Published: 23 October 2023

Copyright: © 2023 by the authors. Licensee MDPI, Basel, Switzerland. This article is an open access article distributed under the terms and conditions of the Creative Commons Attribution (CC BY) license (https://creativecommons.org/licenses/by/4.0/).

1. Introduction

The installation of photovoltaic (PV) power systems has increased in recent years, as an important renewable energy option to meet the growing energy demand and the environmental challenges [1,2]. The general configuration of a single-phase grid-connected PV system with a transformer is depicted in Figure 1. It comprises a PV array, a DC–DC converter, a single-phase inverter, an LCL filter, and a load connected to the grid through a single-phase saturable transformer [3].

Connecting the transformer to the distribution grid or recovering from grid faults can cause high inrush currents through the primary winding when the ferromagnetic core is driven into saturation. Inrush current may lead to undesirable events, such as incorrect operation of protective relays, mechanical damage to the transformer windings, excessive stress on the insulation, and disturbances that can affect the power quality of the grid and neighboring facilities [4–8]. Inrush current is detrimental to utility cables, as the current spike causes a voltage drop in the system. The weaker the transmission/distribution line, the more pronounced this voltage drop will be. This, in turn, potentially causes other loads to drop or even adjacent PV systems to operate with low voltage. If there are several PV systems on a single connected line, there could be a pattern of systemic voltage drops [9]. Grid codes are now being revised worldwide to limit transformer inrush currents. Avoiding inrush currents increases the reliability of a grid-connected PV system and the security and stability of the power grid.

The techniques for inrush current reduction in single-phase transformers can be classified into four general types: (1) external device insertion [10–16], (2) methods that change

the transformer design [17–21], (3) residual flux reduction [22–26], and (4) controlling the energization point-on-wave [27–31]. The first two approaches can be expensive and impractical and do not completely eliminate inrush currents [21].

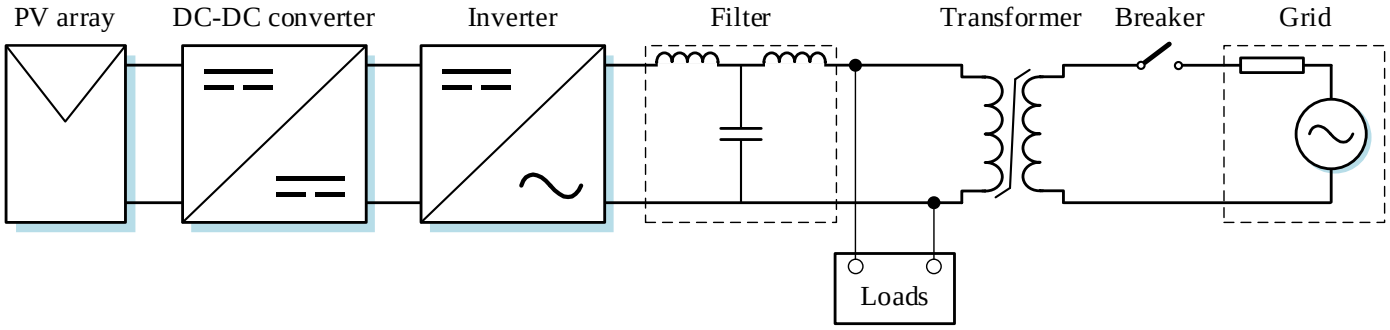

Figure 1. Typical configuration of a single-phase grid-connected PV system.

The last two approaches are intricately linked to each other. When a transformer is de-energized, a residual flux can remain in the iron core due to the hysteresis characteristics of ferromagnetic materials. The determination of the most favorable energization point-on-wave, crucial for avoiding inrush current, relies on the value of this residual flux. The energization point-on-wave and the residual flux (in an indirect manner) are the only controllable parameters among all those on which the inrush current depends.

To achieve controlled energization, prior knowledge of the residual flux is essential. To address this challenge, there have been publications focusing on measuring and estimating the residual flux [32–39], as well as pre-setting a known residual flux value [40]. Since the residual flux can be different before each energization, it becomes necessary to consistently measure or estimate it before energizing the transformer using these approaches. This requires continuously acquiring signals and performing online calculations. Furthermore, most methodologies require specialized equipment and complex setups, typically implemented only in laboratories, resulting in unsuitability for specific applications.

The smart switching for inrush current elimination proposed in this paper avoids the need to measure or estimate the residual flux before each energization, which results in a more simplistic methodology than those in the literature. Figure 2 presents a comparison between the flowchart of common approaches and the proposed smart switching, while Figure 3 provides a comparison between the experimental setups. It can be seen that the proposal is more simplistic and avoids the stages of measuring, eliminating, or presetting the residual flux, with the corresponding savings in specific equipment and/or processing costs.

Removing the need to measure the residual flux is possible by using only two pieces of data (calculated from two no-load tests which characterize the static hysteresis loop and the de-energization flux trajectories): ϕ_{RM} (the flux value of the green point in Figure 4a) and ϕ_0 (the flux value of the red point in Figure 4a), or the corresponding voltage points-on-wave, α_{RM} and α_0, along with an understanding of the used breaker technology.

Although the proposed smart switching is also applicable to SCR and IGBT breakers, the SCR breaker is a more cost-effective solution for large power systems.

The rest of the paper is organized as follows. Section 2 analyses the inrush current phenomenon, along with the residual flux and its de-energization trajectories. It also discusses the essential characteristics required for an accurate simulation of de-energization and inrush current in a transformer model. Section 3 introduces the proposed smart switching to eliminate inrush currents. The results are presented and discussed in Section 4. Finally, Section 5 summarizes the main conclusions.

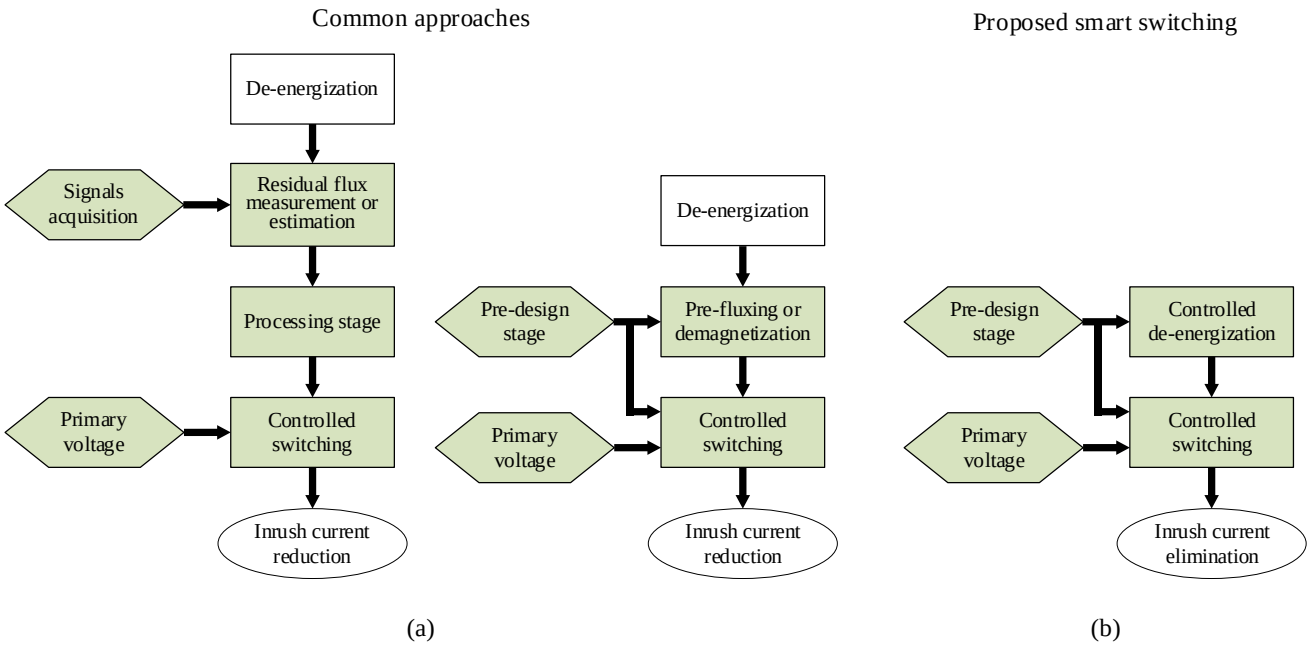

Figure 2. Flowcharts of (**a**) common approaches for inrush current reduction and (**b**) the proposed smart switching for inrush current elimination.

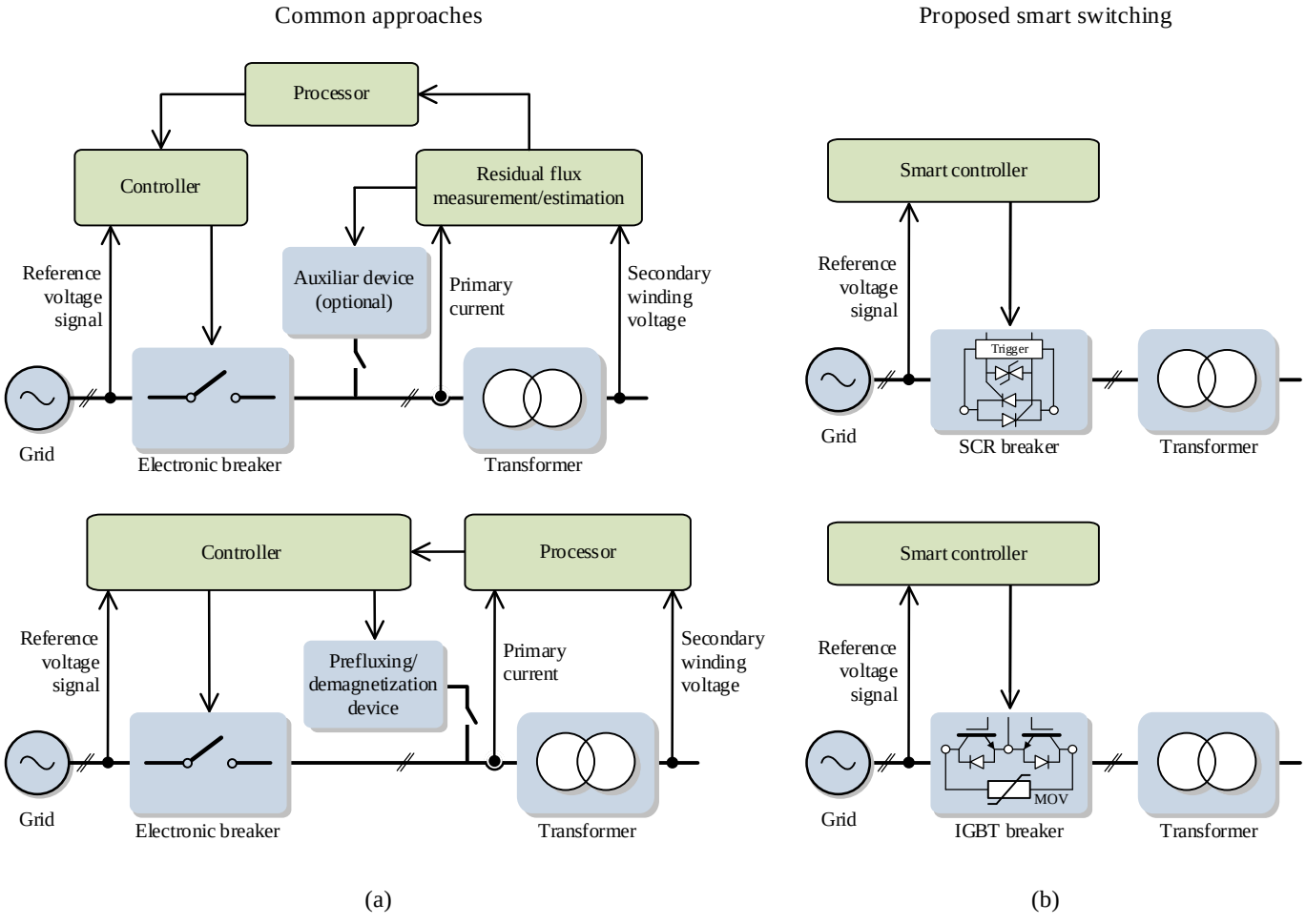

Figure 3. Experimental setups of (**a**) common approaches for inrush current reduction and (**b**) the proposed smart switching for inrush current elimination.

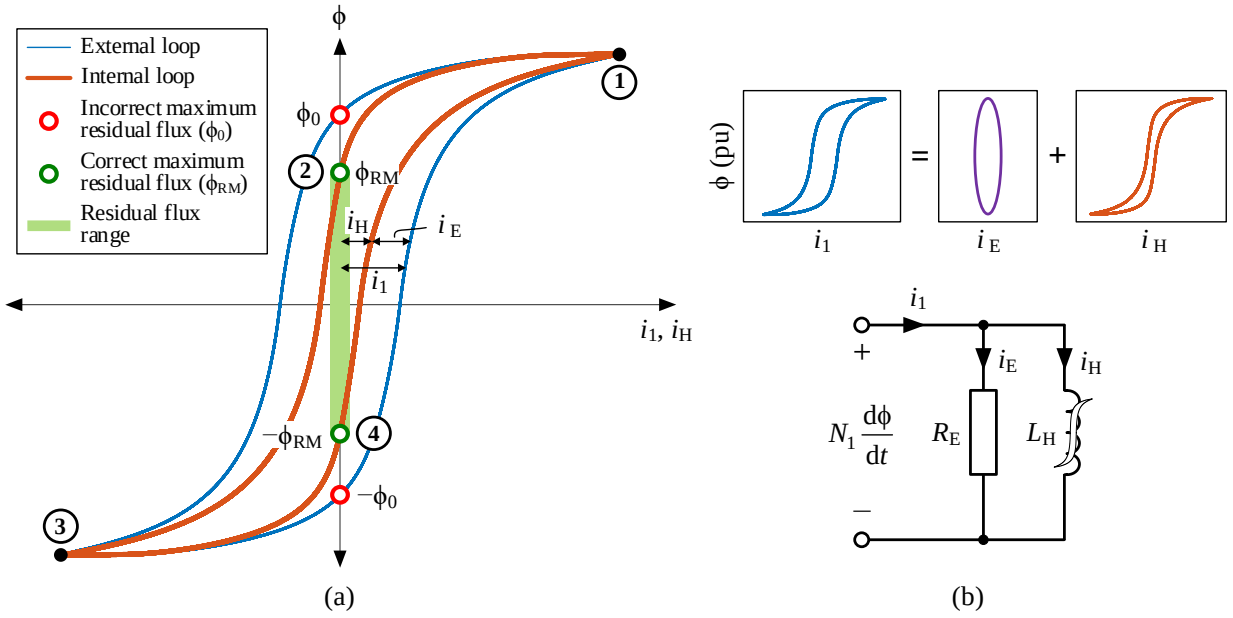

Figure 4. (**a**) External and internal loops and residual flux range. (**b**) Equivalent electric circuit of the transformer core.

2. Analysis of Inrush Current and Residual Flux

2.1. Transformer Models for Residual Flux Prediction

The iron losses in a transformer core can be divided into three general categories: hysteresis losses, classical eddy-current losses, and excess or anomalous losses [41,42]. The hysteresis losses are considered static because their value per cycle does not depend on the frequency. The hysteresis losses are proportional to the involved area within the hysteresis loop, whose evolution depends on past or historical values. The eddy losses are considered dynamic because their value per cycle is frequency dependent [43–45]. As the classical eddy losses and the excess losses do not influence the residual flux, both components are grouped in this paper as eddy losses. Then, the no-load current i_1 is given by the current due to hysteresis losses, i_H, plus the current due to eddy losses, i_E, as shown in Figure 4.

The only way to characterize the residual flux is with a hysteretic core model [46], i.e., a model with a memory-like effect or a storage-like effect. The most common ones are Jiles–Atherton (JA) and Preisach. A correct hysteretic core modeling must include the following components (Figure 4b):

(1) An internal hysteresis loop (red line in Figure 4). This loop is caused by the core magnetization and the hysteresis losses and cannot be directly measured through the classical no-load test. It is commonly referred to as the static hysteresis loop since it is independent of frequency;

(2) An external hysteresis loop (blue line in Figure 4). This loop is directly measurable, and it is composed of the internal hysteresis loop plus the eddy losses. It is referred to as the dynamic loop because of the eddy losses frequency dependence.

A single-phase transformer can be modeled by both an electric and a magnetic circuit. Figure 5 depicts four distinct unloaded single-phase transformer models, all sharing the same electric circuit but featuring different magnetic circuits with various types of core modeling. These differences in core modeling result in varying predictions for residual flux.

The electric circuit includes the winding resistances, R_1 and R_2, the constant leakage inductances, L_{d1} and L_{d2}, and the induced primary voltage, due to the core magnetic flux, ϕ.

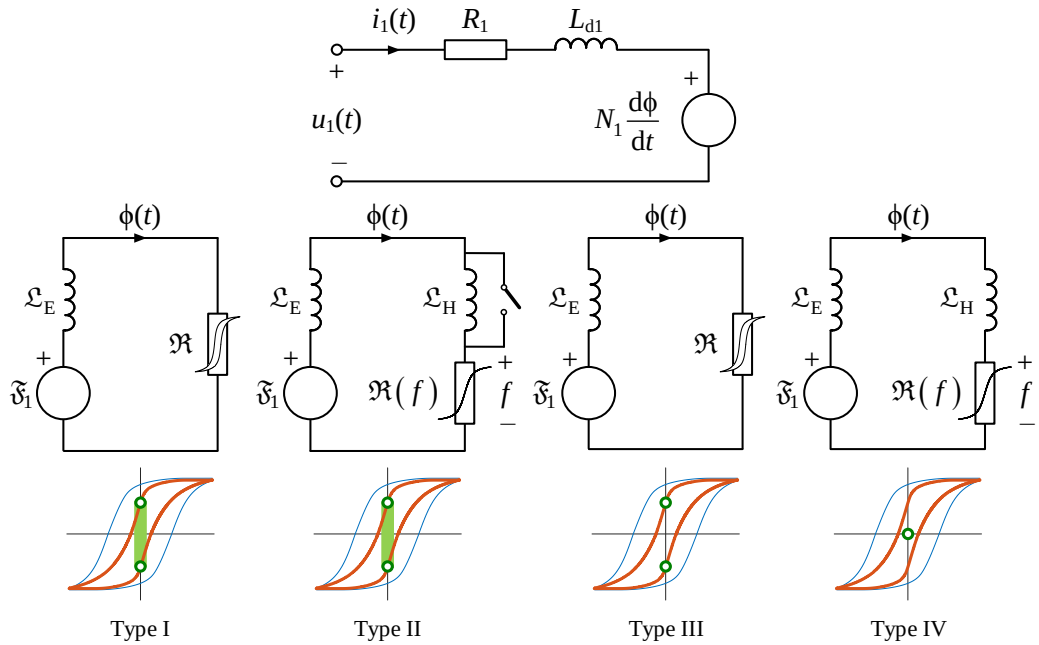

Figure 5. Electric (**top**) and magnetic circuits (**bottom**) of an unloaded single-phase transformer, and residual flux ranges for the four types of models.

As the residual flux is physically retained in the core when the transformer is disconnected, the modeling must also include a storage function to trap such flux. The magnetic inductance (also called transference), $\mathfrak{L}_E$, in the magnetic circuit represents the eddy losses, while $\mathfrak{L}_H$ (only present in Type II and Type IV) represents the internal loop hysteresis losses. Note that the hysteresis losses in Type I and Type III are embedded into a hysteretic nonlinear reluctance $\mathfrak{R}$. The magnetic inductances $\mathfrak{L}_E$ and $\mathfrak{L}_H$ could be placed into the electric circuit as parallel resistances by applying the duality principle [47], as made in most research papers.

The main features of these four types of models are as follows:

- Type I. Reluctance $\mathfrak{R}$ is hysteretic and capable of reproducing major and minor loops, both symmetric and asymmetric ones. JA and Preisach models, in their original static versions, are the best examples of this type. This type of model can accurately predict all the residual flux values inside the allowable range;
- Type II. Non-hysteretic reluctance $\mathfrak{R}$ is able to reproduce major loops when combined with $\mathfrak{L}_H$. The set composed of $\mathfrak{L}_H$ and the magnetic switch provides the memory and storing features to this model. If the magnetic switch is closed due to a transformer de-energization event, the current through $\mathfrak{L}_H$ (representing the residual flux) will continue circulating indefinitely. The magnetic switch is closed when the following conditions are met simultaneously: current i_1 is null and magnetic potential at $\mathfrak{L}_H$ is null. This model predicts the residual flux values inside the allowable range;
- Type III. Hysteretic reluctance $\mathfrak{R}$ can only reproduce a unique and rigid major loop [48]. Inevitably, this model can only lead to the maximum or minimum residual flux values;
- Type IV. Non-hysteretic reluctance, $\mathfrak{R}$, can reproduce major loops when combined with $\mathfrak{L}_H$. This model always leads to a null residual flux value.

Only the Type I (with JA and Preisach) model is used in this paper. JA and Preisach hysteresis models are detailed in Appendix A.

2.2. Residual Flux and De-Energization Trajectories

This section describes the trajectories during the de-energization transient. To the authors' knowledge, these trajectories are not sufficiently well explained in the literature, especially when the residual flux range is of concern.

Figure 6 illustrates two representative de-energization transient trajectories. Let us now consider that the circuit breaker aperture starts at the instant marked with a blue circle in Figure 6a. The flux trajectory follows the major loop illustrated in the figure until the residual flux reaches the value ϕ_{RM}. Note that only the internal hysteresis loop has been taken into account because the eddy losses do not influence the achieved residual flux.

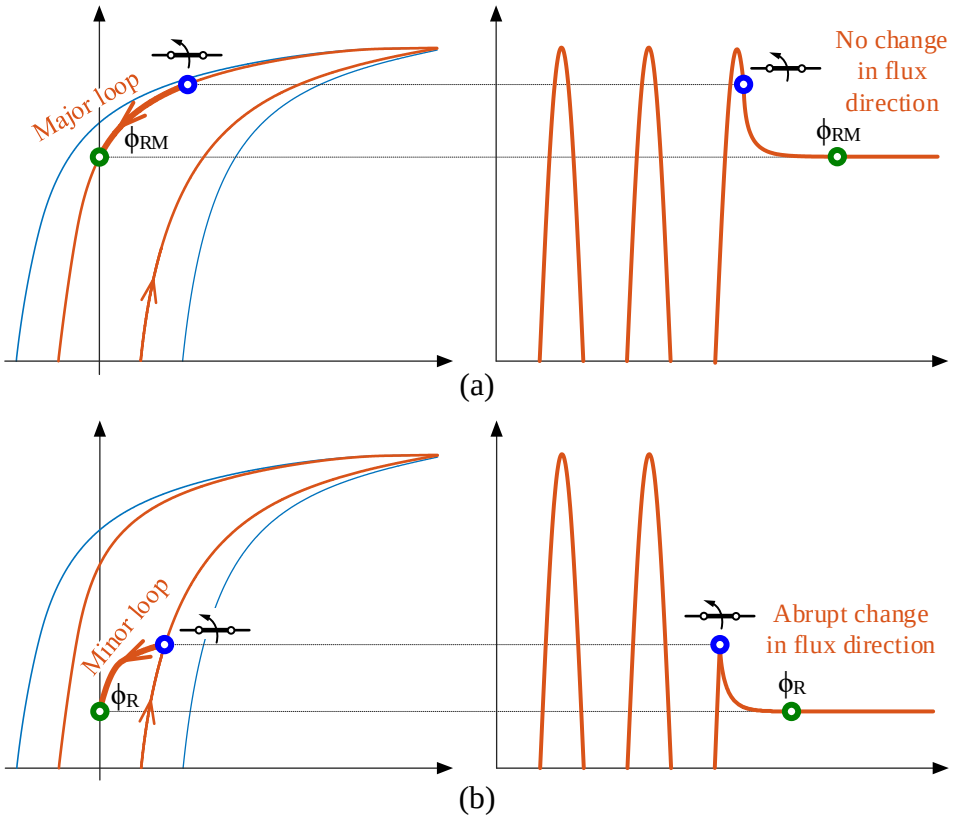

Figure 6. Two de-energization transient trajectories and their respective flux waveforms: (**a**) major loop and (**b**) minor loop.

In the example in Figure 6b, the circuit breaker aperture initiates at a different instant. In this case, the flux follows the trajectory of an asymmetric minor loop until the residual flux reaches a value ϕ_R, which is smaller than ϕ_{RM}.

The above two examples are representative of all de-energization transients in the hysteresis loop:

(1) Transients that follow the major loop because the breaker aperture does not provoke a change in flux direction;
(2) Transients that follow an asymmetric minor loop because the breaker aperture provokes an abrupt change in flux direction.

Based on this, four different regions in the hysteresis loop can be highlighted. Each zone leads to different well defined residual flux values because the transience in the hysteresis loop depends only on the instant of breaker aperture initiation. This instant of aperture initiation is best characterized by the corresponding supply voltage point-on-wave (with reference to the maximum of the voltage) and is called herein the de-energization point-on-wave, α_D.

If the disconnection starts at point-on-wave, α_D, between 90° and α_{RM} (between points 1 and 2 in Figure 4), the residual flux will always be ϕ_{RM}. On the contrary, the residual flux will always be $-\phi_{RM}$ if the switching point-on-wave is between 270° and 270° + α_{RM} (between points 3 and 4). The values of α_{RM} and 270° + α_{RM} vary for each transformer and

depend on core parameters. Their values are calculated from the no-load tests detailed in Section 3.2.

The possible residual flux values in the remaining two zones are as follows. If α_D is between α_{RM} and 270° (between points 2 and 3), the residual flux reaches a value between ϕ_{RM} and $-\phi_{RM}$ (green stripe in Figure 4). However, there is no ambiguity, as the specific value will be uniquely defined by the specific minor loop trajectory which follows, which will depend only on α_D. The opposite happens for the region between 270° + α_{RM} and 90° (between points 4 and 1): the residual flux reaches a value within the range $-\phi_{RM}$ to ϕ_{RM}. This dependence on de-energization point-on-wave is shown in Table 1.

Table 1. Possible residual flux values.

Points on Figure 4	De-Energization Point-on-Wave α_D	Residual Flux Range ϕ_R	Trajectory
1 to 2	90° to α_{RM}	ϕ_{RM}	Major loop
2 to 3	α_{RM} to 270°	ϕ_{RM} to $-\phi_{RM}$	Minor loop
3 to 4	270° to 270 + α_{RM}	$-\phi_{RM}$	Major loop
4 to 1	270 + α_{RM} to 90°	$-\phi_{RM}$ to ϕ_{RM}	Minor loop

Figure 7 illustrates two de-energization trajectories at two different circuit breaker interruption speeds. It can be seen that the interruption speed only influences the de-energization trajectory of the external loop and the decaying time of i_1. In contrast, the de-energization trajectory of the internal loop and the decay time of i_H are uniquely determined by the hysteretic reluctance (e.g., that in the Type I model in Figure 5). Thus, the residual flux reached is the same for both breaker speeds. As the residual flux only depends on i_H, the interruption speed and the eddy losses have no influence on the residual flux ϕ_R. This is also stated in [49] as follows: "the residual flux pattern is determined by static characteristics of the core". In summary, it can be said that, once the current begins to be interrupted and the flux begins to decay, the value of the future residual flux is already predetermined.

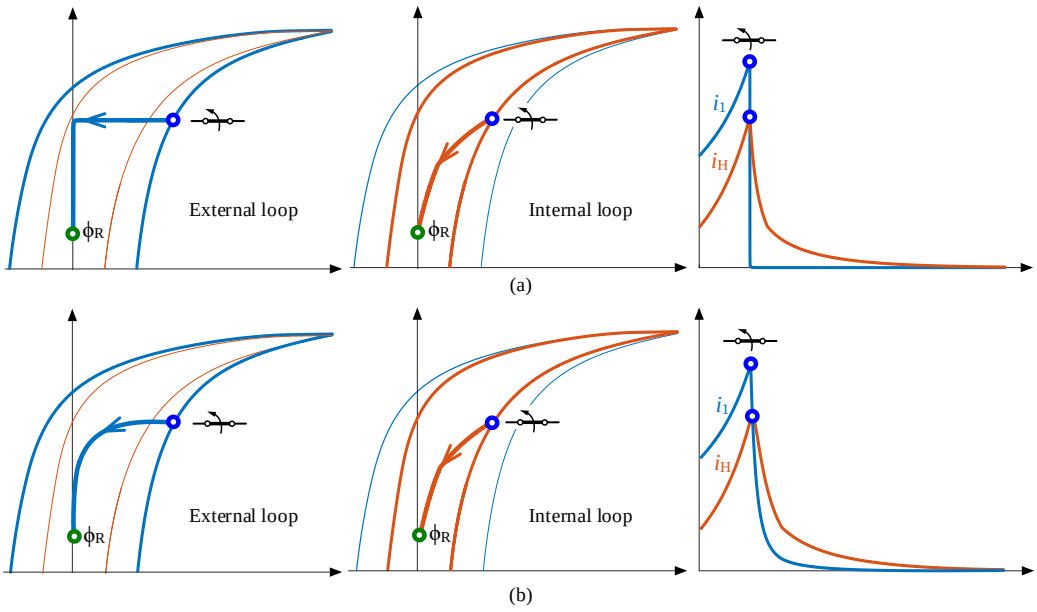

Figure 7. De-energization trajectories and their respective current waveforms (i_1 and i_H) at two different interruption speeds of the circuit breaker: (**a**) abrupt interruption and (**b**) soft interruption.

3. Inrush Current Elimination

3.1. Circuit Breakers

Current chopping (or simply chopping) in a circuit breaker is the phenomenon in which the current is forcibly interrupted before the natural current zero-crossing. In power systems, the vacuum or SF6 circuit breakers and the unused air blast circuit breakers have chopping capability. In contrast, the old and unused oil circuit breakers do not have chopping capability.

In this paper, three different circuit breakers have been used to de-energize and energize the tested transformers:

1. SCR-based breaker: Semiconductor breaker composed of two antiparallel silicon-controlled rectifiers. Once the trip signal is sent, the current is not interrupted until its natural zero-crossing, and this happens regardless of the load nature (resistive or inductive). As a consequence, no electric arc is produced. This null chopping capability can be assimilated to that in oil breakers;
2. Electro-mechanical contactor: Circuit breaker with chopping capability. If the load is inductive, an electric arc is produced and the interruption will not be instantaneous, but the current will be brought to zero before its natural current zero-crossing. This chopping capability can be assimilated to that in vacuum or SF6 breakers;
3. IGBT-based breaker: Semiconductor breaker composed of two IGBTs (each one with an antiparallel diode) connected in series with a common emitter. It has high chopping capability, with a low clearance time at any instant, regardless of the nature of the load. No electric arc is produced. Its high chopping capability cannot be assimilated into any power system breaker.

There is a time lapse between the trip signal and the start of the breaker opening (or de-energization point-on-wave). In the SCR breaker, this delay is on the order of hundreds of microseconds. Thus, the trip signal must be sent, at least, around 10° before the desired zero-crossing. In the IGBT breaker, the delay is in the order of microseconds. Then, this delay can be neglected in the IGBT breaker, and trip signal and point-on-wave terms can be used indistinctly. In the contactor, the delay could be on the order of several milliseconds (5 to 10 milliseconds). This delay is undetermined because it depends on the instant at which the trip signal is sent. Thus, the de-energization point-on-wave cannot be controlled in the contactor.

3.2. Smart Switching for Inrush Current Elimination

Power transformers are typically designed to operate slightly above the knee point of the saturation curve. A slight increase in flux beyond this point leads to a noticeable rise in magnetizing current. After the energization, the maximum theoretical flux peak can reach two times the rated flux peak plus the residual flux, $\phi_{MAX} = 2\phi_{PEAK} + \phi_R = 2\cdot\sqrt{2}\phi_N + \phi_R$, if the primary winding resistance and the primary leakage inductance are neglected.

The basic principle to eliminate flux asymmetry and thereby minimize inrush currents is to ensure that the prospective flux at energization matches the residual flux. Thus, the optimal energization point-on-wave occurs when the prospective flux equals the residual flux. Although there are two energization points-on-wave for each residual flux value, for simplicity, only one of them will be considered in this paper.

It has been shown that the residual flux is only determined by the de-energization trajectory, which is only influenced by the de-energization point-on-wave. Therefore, the magnitude of the inrush current can be determined by controlling the de-energization and energization points-on-wave.

The proposed strategy comprises two steps. First, forcing that the residual flux after de-energization is at its maximum value (ϕ_{RM} or $-\phi_{RM}$). For simplicity, only ϕ_{RM} is considered in this paper. The second step is to energize the transformer at the optimum energization point-on-wave for ϕ_{RM}. It is proposed to use ϕ_{RM} because this value can be accurately determined as the crossing of the internal hysteresis loop with the positive vertical axis.

The next issue is the determination of the internal loop by the following straightforward method: a no-load test at nominal frequency and a second test at another frequency. Both tests must be made at rated flux. To maintain rated flux in the core, the supply voltage must be $U = U_N \cdot (f/f_N)$. Then, i_H can be calculated according to

$$i_H = i_1 - i_E = i_1 - \frac{u_1}{R_E} = i_1 - \frac{u_1}{\Delta U/\Delta I} \quad (1)$$

where u_1 and i_1 are the primary voltage and current from the nominal frequency test, and $\Delta U/\Delta I$ is the ratio of change of primary voltage and current between both tests. Alternatively, these two frequency no-load tests can be replaced by only one no-load test at a very low frequency f (e.g., 2 Hz). This low-frequency test provides the internal loop as $i_1 \approx i_H$, and it must be made at rated flux.

To force ϕ_{RM}, the de-energization point-on-wave α_D must be between 90° and α_{RM} (Table 1). The angle α_{RM} can be obtained as

$$\alpha_{RM} = 180^\circ - \operatorname{asin}\left(\frac{\phi_{RM}}{\phi_{N\,PEAK}}\right) \approx 180^\circ - \operatorname{asin}\left(\frac{\omega\phi_{RM}}{\sqrt{2}U_N}\right) \quad (2)$$

The current interruption of a no-load transformer with an IGBT breaker can provoke large overvoltages because the interruption of this breaker is typically abrupt. These overvoltages can damage the transformer isolation. To avoid this, the de-energization trip signal must be sent to the IGBT breaker when the current is near zero (see Figure 8). This de-energization point-on-wave, α_0, can be calculated as

$$\alpha_0 = 180^\circ - \operatorname{asin}\left(\frac{\phi_0}{\phi_{PEAK}}\right) \approx 180^\circ - \operatorname{asin}\left(\frac{\omega\phi_0}{\sqrt{2}U_1}\right) \quad (3)$$

where ϕ_0 is the instantaneous flux when i_1 is null, whose value can be obtained from the external loop.

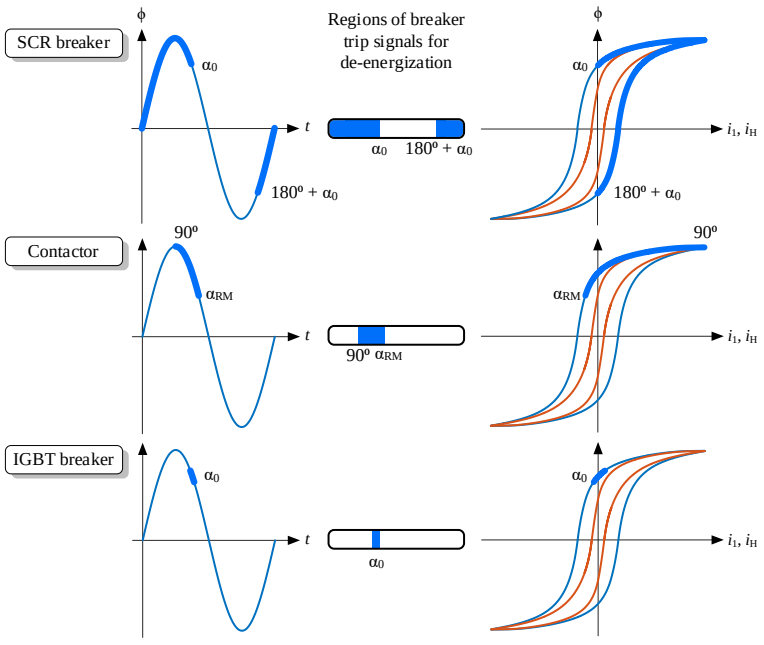

Figure 8. Regions of the hysteresis loop where the trip signal must be sent to each breaker.

In the case of the contactor, the current interruption is not abrupt. Thus, no overvoltages are produced and α_D can take any value between 90° and α_{RM} (see Figure 8). Althought α_D cannot be controlled in the contactor, the study of its behavior is profitable because its chopping capability can be assimilated to that of vacuum and SF6 power system breakers.

Finally, the trip signal of the SCR breaker can be sent at any instant because there are only two possible de-energization points-on-wave (see Figure 8). As a consequence, residual fluxes $-\phi_{RM}$ and ϕ_{RM} will always be achieved.

On the other hand, neglecting the primary winding resistance and the primary leakage inductance, the flux after energization is given by

$$\phi = \phi_R + \frac{\sqrt{2}U_1}{\omega}[\sin(\omega t) - \sin(\alpha_E)] \tag{4}$$

which illustrates that the energization transient flux is affected by the energization point-on-wave, α_E, and ϕ_R. To avoid the subsequent inrush current, the offset in Equation (4) must be null. Then, if ϕ_R is equal to ϕ_{RM}, the optimal α_E is

$$\alpha_E = 180^\circ - \operatorname{asin}\left(\frac{\phi_{RM}}{\phi_{PEAK}}\right) = \alpha_{RM} \tag{5}$$

A whole smart switching strategy to avoid inrush current in single-phase transformers of PV systems is illustrated in Figure 9 and summarized in Table 2.

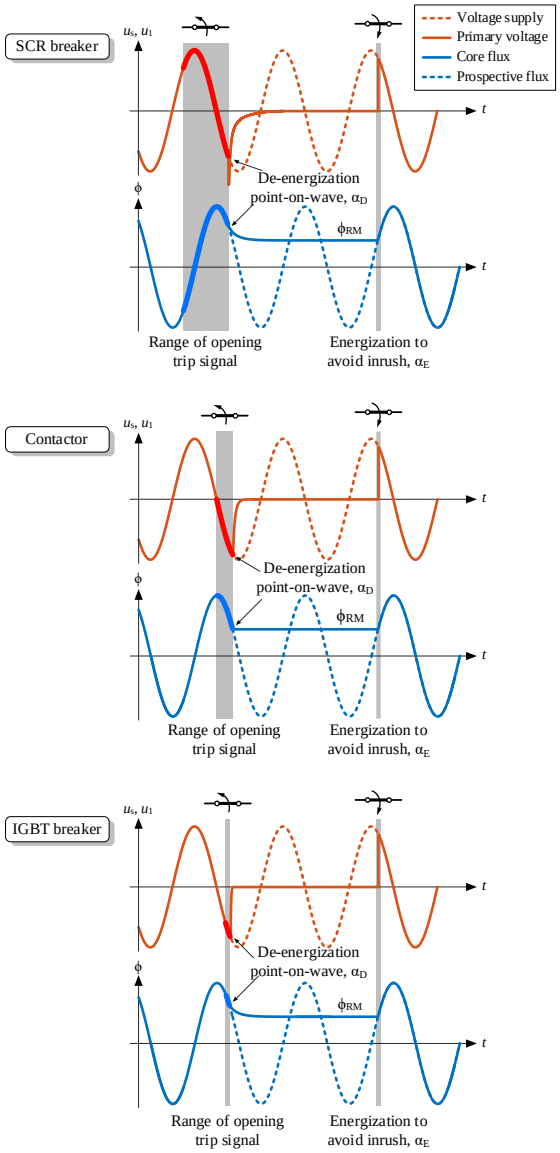

Figure 9. De-energization and energization strategy to avoid inrush current. Opening and closing regions for each breaker.

Table 2. Smart switching to avoid inrush currents.

Laboratory Tested Breakers	Equivalent Power System Breakers	Trip Signal	De-Energization Point-on-Wave, α_D	Residual Flux	Energization Points-on-Wave, α_E
SCR breaker	Oil breakers Vacuum and SF6 breakers	$180^\circ + \alpha_0$ to α_0	α_0	ϕ_{RM}	α_{RM}
Contactor		90° to α_{RM} *	90° to α_{RM}	ϕ_{RM}	α_{RM}
IGBT breaker	-	α_0	α_0	ϕ_{RM}	α_{RM}

* Neglecting the delay between the trip signal and α_D.

Finally, if the de-energization cannot be controlled, a compromise solution must be adopted: the recommendation is to energize at a point-on-wave of 0° (when the voltage is at its positive peak). This energization point-on-wave is optimal to avoid inrush current when ϕ_R is null. Thus, the flux peak will be equal to or lower than $\phi_{MAX} = \phi_{PEAK} + \phi_R = \sqrt{2}\phi_N + \phi_R$.

4. Experimental Results and Discussion

The analysis of the residual flux and its de-energization trajectories was supported by several experiments conducted on two different single-phase transformers of 320 VA, 120/72 V, short-circuit reactance 0.046, and 0.07 pu, which are denoted as T1 and T2. Each experiment consists of two stages: (a) transformer de-energization at a desired point-on-wave and (b) transformer energization at upward zero-crossing of the voltage, which results in the most severe positive inrush current when ϕ_R is null. As the residual flux cannot be measured directly, it has been estimated offline using the resultant inrush, as proposed in [50]. The IGBT and SCR breakers have been used because the absence of electric arc allows a clearer comprehension of the residual flux phenomenon. In each experiment, α_D is varied from 0° to 360° in steps of 10°. The subsequent energizations have been achieved at a constant $\alpha_E = 270^\circ$, in order to validate the residual flux value. It can be verified that the results are consistent with the residual flux analysis discussed in Section 2.2. The maximum residual flux value, obtained from the mentioned frequency no-load tests in Section 3.2 and using Equation (1) is $\phi_{RM} = 0.326$ pu for T1 and $\phi_{RM} = 0.344$ pu for T2. These values fall within the typical range established for small transformers in [46]. From Equation (2), it is calculated that, when the energization point-on-wave when IGBT breaker is used, $\alpha_{RM} = 166.7^\circ$ for T1 and $\alpha_{RM} = 165.9^\circ$ for T2. From the classical no-load test, it is determined that the instantaneous flux value, when i_1 is null (crossing between the vertical axis and the external loop), is $\phi_0 = 1$ pu for T1 and $\phi_0 = 0.94$ pu for T2. Lastly, Equation (3) yields the de-energization point-on-wave $\alpha_0 = 132.5^\circ$ for T1 and $\alpha_0 = 138.4^\circ$ for T2.

The results corroborate the dependence of the residual flux on α_D and also corroborate that there is no dependence on the interruption speed. Some external loops and the corresponding external de-energization trajectories obtained during the experiments with the IGBT and SCR breakers are depicted in Figure 10 and Figure 11, respectively.

The obtained inrush currents in the experiments with the SCR breaker were always of the same amplitude. These results confirm that the de-energization with the SCR breaker always leads to residual fluxes $-\phi_{RM}$ and ϕ_{RM}.

Transformers T1 and T2 have also been simulated in the Matlab environment to validate the residual flux values obtained experimentally, each one with a JA and a Preisach core model, as these two models are able to adequately represent the residual flux behavior.

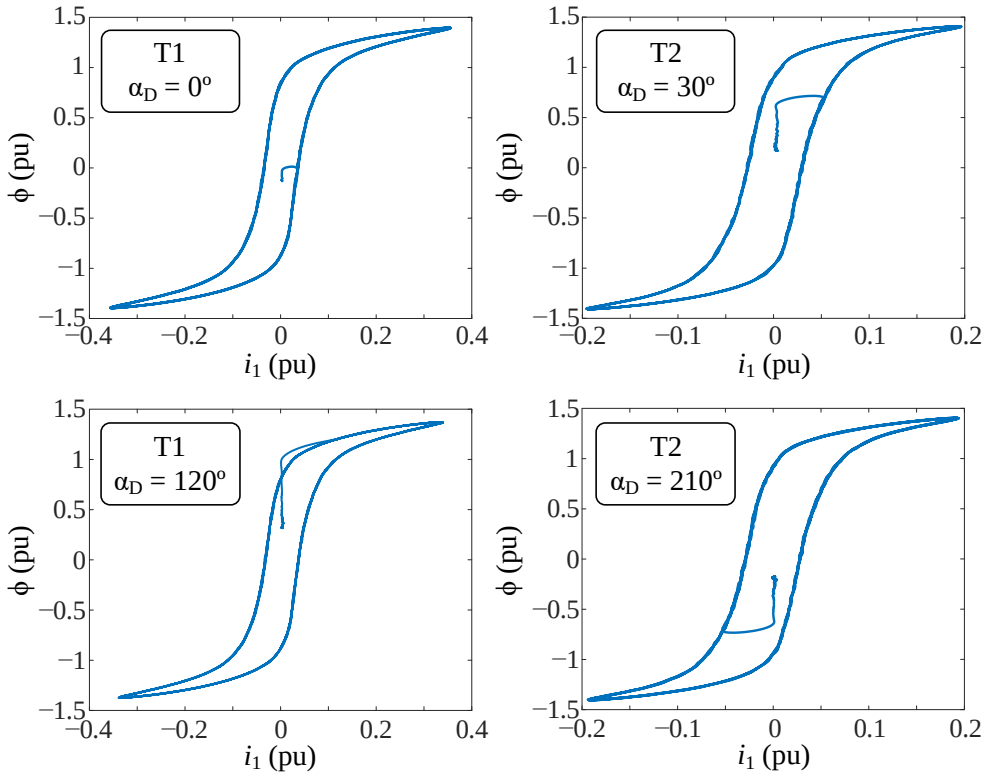

Figure 10. Measured external loops and de-energization trajectories when the IGBT breaker is used.

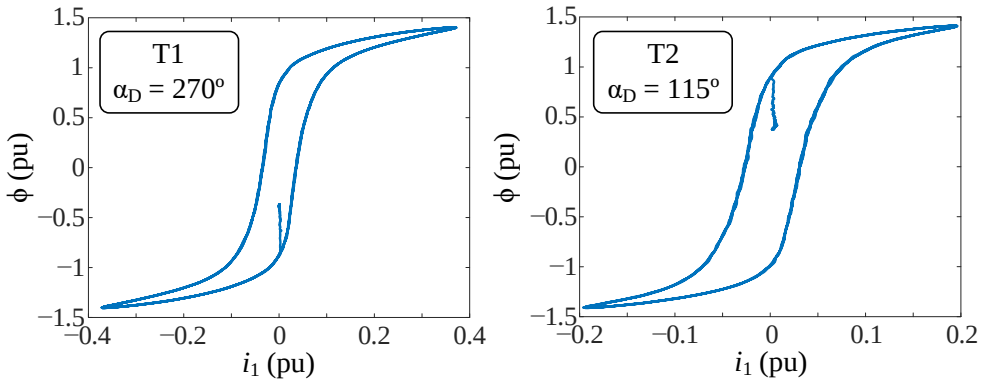

Figure 11. Measured external loops and de-energization trajectories when the SCR breaker is used.

The value of $\mathfrak{L}_E$ is calculated from the previously mentioned two no-load tests (Section 3.2) at two different frequencies with the same flux level:

$$\mathfrak{L}_E = \frac{{N_1}^2}{R_E} = \frac{{N_1}^2}{\Delta U/\Delta I} \tag{6}$$

where N_1 is the number of primary winding turns. The winding parameters, R_1, R_2, L_{d1}, and L_{d2}, have been estimated with the classical short-circuit test.

The JA model parameters have been adjusted manually. The Preisach Distribution Functions (PDFs) of the Preisach models have been calculated with the centered cycles method [51]. This method uses a set of steady-state symmetrical internal loops at different voltages. The internal loops are obtained as explained in Section 3.2.

In all simulations, the circuit breaker is supposed to be ideal (close to the behavior of the IGBT breaker). Figure 12 shows the residual flux values as a function of α_D, obtained from JA and Preisach simulations, as well as the values estimated from the experiments.

There is close agreement between experiments and simulations, and the results validate the presented analyses of the residual flux and the de-energization trajectories.

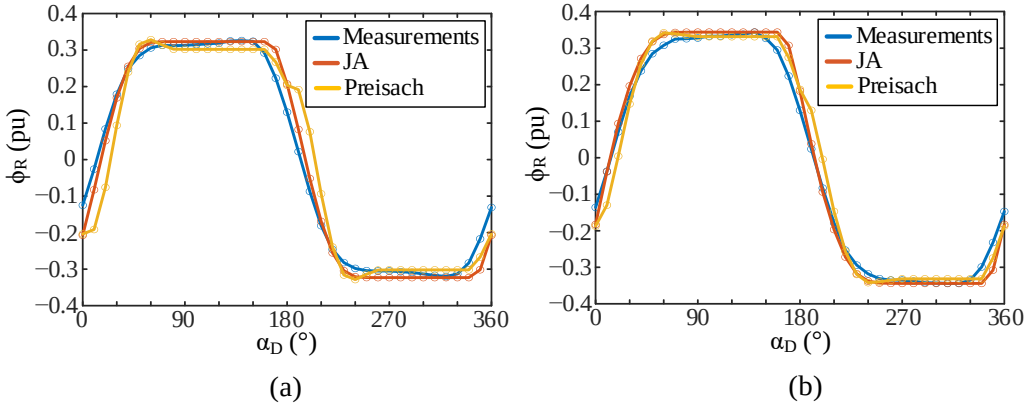

Figure 12. Residual flux values in function of the de-energization point-on-wave: (**a**) T1, (**b**) T2.

The Jiles–Atherton and Preisach hysteresis models have yielded accurate predictions of the residual flux, even when parameter estimation in both models has been based on limited information (only from no-load tests). The inclusion of additional information from asymmetric minor loops in the parameter estimation process does not result in significant improvements in the prediction of residual fluxes.

The proposed strategy to avoid large inrush currents was validated for the SCR and the IGBT breakers. Figure 13 shows inrush currents of different severity for transformer T1 with a de-energization point-on-wave $\alpha_D = 90°$. In this figure, both switchings have been made with the SCR breaker. Figure 13a corresponds to the worst case of inrush current (around 12 pu), as the energization point-on-wave is $\alpha_E = 270°$. It is important to take into account that, for large transformers, the maximum residual flux values are larger (around 0.7 pu) and the resulting inrush currents with this approach can be more severe. Figure 13b shows the resulting currents with the proposed smart switching using the SCR and the IGBT breakers. As can be seen, there is no overcurrent.

Lastly, Figure 14 depicts the compromise solution (energization point-on-wave $\alpha_E = 0°$) when the de-energization cannot be controlled. The inrush current is less severe, with a first peak around 1 pu. This demonstrates that good results can be obtained even with uncontrolled de-energization when the energization is adequately controlled.

The measurements and simulations results validate the following:

1. The residual flux values are bounded by the internal hysteresis loop, i.e., between $-\phi_{RM}$ and ϕ_{RM}. The maximum residual flux value, ϕ_{RM}, is not given by the red point in Figure 4, but by the green point, i.e., ϕ_0 is not ϕ_{RM}. Note that ϕ_{RM} is incorrectly marked in many textbooks as the red point in Figure 4;
2. The eddy losses do not influence the residual flux;
3. The residual flux is independent of the interruption speed of the circuit breaker and solely depends on the starting point of de-energization;
4. The proposed smart switching for de-energization and subsequent energization efficiently avoids the inrush currents through a more simplistic method than those in the literature;
5. The smart switching only requires two pieces of data (obtained from only two simple no-load tests, which characterize the static hysteresis loop and the dynamic loop): ϕ_{RM} and ϕ_0, or the corresponding voltage points-on-wave α_{RM} and α_0, along with understanding of the used breaker technology.

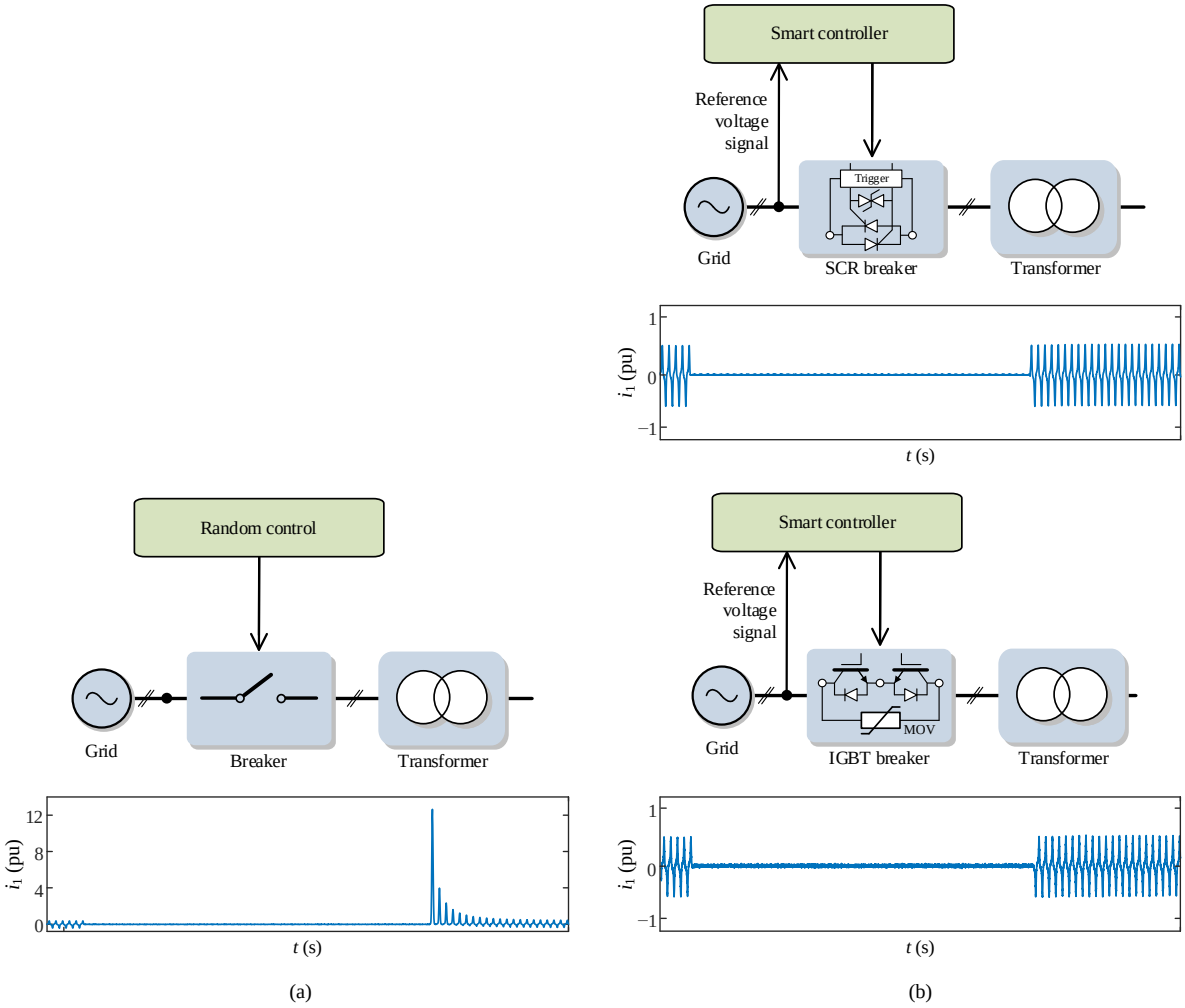

Figure 13. (**a**) Experimental inrush current resulting from random switching with T1, (**b**) experimental current resulting from smart switching with T1.

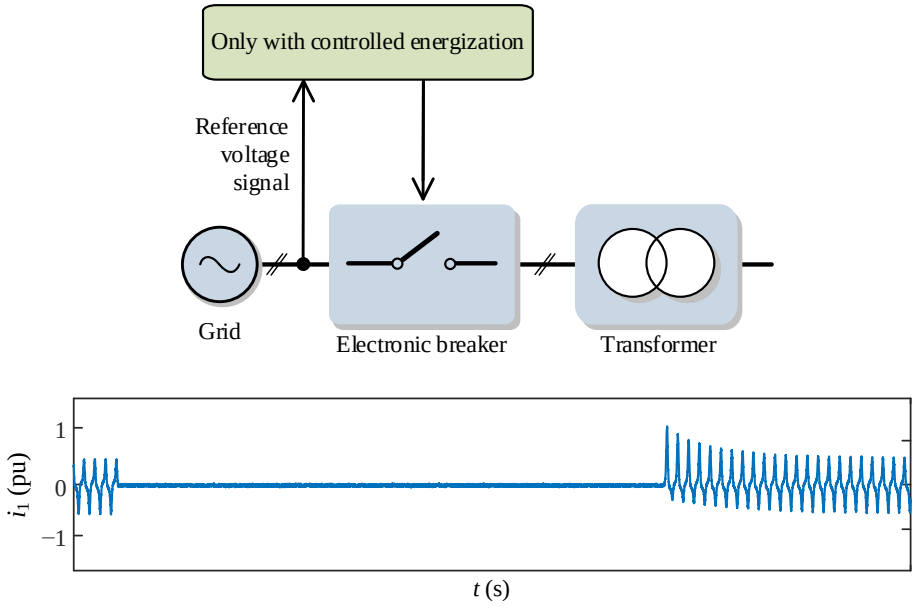

Figure 14. Experimental current with the compromise solution: only controlled energization at $\alpha_E = 0°$, without controlled de-energization or prior residual flux knowledge.

The proposed smart switching can also be implemented, without modifications, to a three-phase PV system only if the transformer is a three-phase bank (three single-phase units) with a star–star connection. However, if the transformer is of the three-legged type, or there is a delta connection, the proposal cannot be directly implemented as described in this paper. Major changes would be necessary, although the theory regarding residual flux and de-energization trajectories remains the same.

5. Conclusions

The transient de-energization trajectories of the transformer have been analyzed in this paper for three main purposes: (1) understanding its behavior, (2) predicting residual flux values, and (3) to propose a smart switching methodology to avoid inrush currents in single-phase grid-connected PV systems that is more simplistic than the literature methodologies.

Regarding the first point, in this paper, it has been demonstrated that (a) the range of residual flux values is determined by the internal hysteresis loop, while eddy losses have no influence, and (b) the residual flux value is independent of the circuit breaker interruption speed and only depends on the de-energization point-on-wave.

The proposed smart switching only requires two pieces of data (obtained from only two simple no-load tests): ϕ_{RM} and ϕ_0, or the corresponding voltage points-on-wave α_{RM} and α_0, along with understanding of the used breaker technology. Opposite to the literature methodologies, the proposed strategy does not require one to estimate the residual flux or to preset a known value before each energization, avoiding complex measurement setups and continuous signal acquisition during each de-energization. It can be applied to any power transformer installed on the grid or in industrial facilities, extending beyond transformers in laboratories.

The implementation of the smart switching increases the reliability of a grid-connected PV system. This approach effectively reduces mechanical stress and other hazardous effects experienced by the transformer, protecting them from damage and prolonging their operating life. Additionally, voltage fluctuations in the grid are substantially reduced and false tripping of protective relays is prevented, ensuring a more stable power supply. This, in turn, safeguards voltage-sensitive loads from interruptions.

Although the proposed smart switching is applicable to SCR and IGBT breakers with equal results, the SCR breaker is a more cost-effective suitable solution for large power systems.

Author Contributions: Conceptualization, G.d.J.M.-F., S.B. and F.C.; methodology, G.d.J.M.-F.; software, G.d.J.M.-F.; validation, G.d.J.M.-F.; formal analysis, G.d.J.M.-F.; investigation, G.d.J.M.-F., S.B. and F.C.; resources, S.B. and F.C.; data curation, G.d.J.M.-F., S.B. and F.C.; writing—original draft preparation, G.d.J.M.-F.; writing—review and editing, S.B. and F.C.; visualization, S.B. and F.C.; supervision, S.B. and F.C.; project administration, S.B. and F.C. All authors have read and agreed to the published version of the manuscript.

Funding: This research received no external funding.

Data Availability Statement: Not applicable.

Acknowledgments: This work was partially supported by the Mexican Council of Science and Technology (CONACyT) by the scholarship 739523.

Conflicts of Interest: The authors declare no conflict of interest.

Appendix A. Transformer Core Models

Appendix A.1. Static Jiles–Atherton Model

The general relation among the flux density, B, the magnetization, M, and the magnetic field intensity, H, is

$$B = \mu_0(H + M) \tag{A1}$$

where μ_0 is the vacuum magnetic permeability. The JA model describes the relation between M and H by using an anhysteretic curve $M_{an} - H_{eff}$ (anhysteretic magnetization as a function of the effective field strength). The original JA model uses a modified Langevin function for this anhysteretic curve. This paper uses the function proposed in [52] for a better fit of the hysteresis loop because it depends on more parameters than the modified Langevin function:

$$M_{an} = \text{sgn}(H_{eff}) \left[\frac{a_1 |H_{eff}| + |H_{eff}|^b}{a_3 + a_2 |H_{eff}| + |H_{eff}|^b} \right] M_s \tag{A2}$$

where M_s is the saturation magnetization and a_1, a_2, a_3, and b are positive constants, with two constraints: $a_2 \geq a_1$ and b must be a positive integer (with a common value of 2).

The JA model is defined by the following differential equation [52–55]:

$$\begin{gathered} \frac{dM}{dH} = \frac{c \frac{dM_{an}}{dH_{eff}} + \frac{\delta_M (M_{an} - M)}{\frac{\delta k}{\mu_0} - \frac{\alpha (M_{an} - M)}{1-c}}}{1 - \alpha c \frac{dM_{an}}{dH_{eff}}} \\ H_{eff} = H + \alpha M \end{gathered} \tag{A3}$$

where α, c, and k are parameters and δ_M and δ are calculated as follows [52–55]:

$$\begin{gathered} \delta_M = \begin{cases} 0 & \text{if } H < 0 \quad \text{and} \quad M_{an} - M \geq 0 \\ 0 & \text{if } H \geq 0 \quad \text{and} \quad M_{an} - M \leq 0 \\ 1 & \text{otherwise} \end{cases} \\ \delta = \begin{cases} 1 & \text{if } H \geq 0 \\ -1 & \text{otherwise} \end{cases} \end{gathered} \tag{A4}$$

Appendix A.2. Static Preisach Model

The main idea of the Preisach model is that the magnetic field in a ferromagnetic material can be considered as a set of elementary hysteresis loops called *hysterons*, which only have two states: +1 and −1. They are illustrated in Figure A1. A switching field couple, which can be expressed by the plane (α, β), characterizes a hysteron. Representing the saturation flux density and saturation magnetic field intensity as B_{SAT} and H_{SAT}, respectively, when $H = H_{SAT}$, all hysterons are positive and the flux density is $B = B_{SAT}$. At the other tip of the loop, if $H = -H_{SAT}$, all hysterons are negative and $B = -B_{SAT}$. This means that α and β are bounded to the range $[-H_{SAT}, H_{SAT}]$. As hysteresis is an energetically dissipative phenomenon, the following constraint must be accomplished: $\alpha \geq \beta$. These conditions define a triangle in the plane (α, β), known as the Preisach triangle, depicted in Figure A1b.

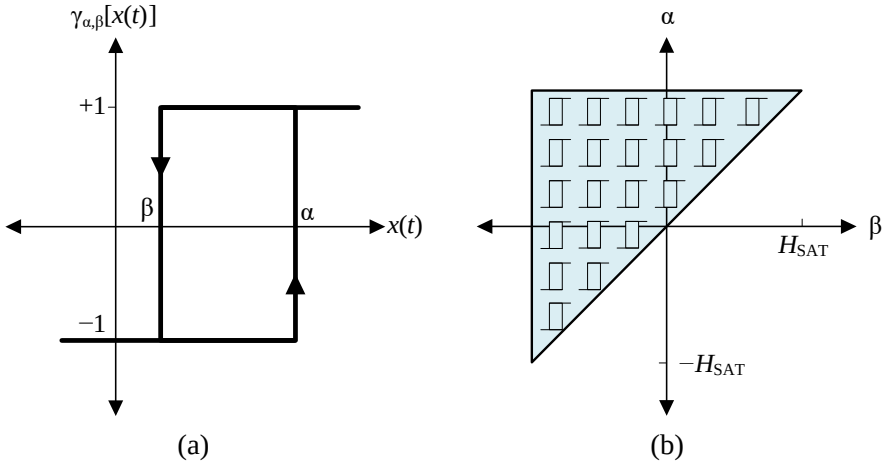

Figure A1. (**a**) Generic diagram of a hysteresis operator. (**b**) Preisach triangle.

The static Preisach model can be defined mathematically by a surface integral as follows [56–58]:

$$B = \iint_{\alpha \geq \beta} \mu(\alpha, \beta) \gamma_{\alpha,\beta}(H) \mathrm{d}\alpha \, \mathrm{d}\beta \tag{A5}$$

where $\gamma_{\alpha,\beta}(\,)$ is the operator associated with each hysteron and $\mu(\alpha,\beta)$ is the Preisach Distribution Function (PDF), which depends on the core and determines the weight of each hysteron. The value of $\gamma_{\alpha,\beta}$ depends on the actual input, $H(t)$, and the previous state and is defined as [56–58]

$$\gamma_{\alpha,\beta}(H) = \begin{cases} +1 & H > \alpha \\ \text{previous output} & \beta < H < \alpha \\ -1 & H < \beta \end{cases} \tag{A6}$$

References

1. Shahsavari, A.; Akbari, M. Potential of solar energy in developing countries for reducing energy-related emissions. *Renew. Sustain. Energy Rev.* **2018**, *90*, 275–291. [CrossRef]
2. Mârza, C.; Moldovan, R.; Corsiuc, G.; Chisăliță, G. Improving the Energy Performance of a Household Using Solar Energy: A Case Study. *Energies* **2023**, *16*, 6423. [CrossRef]
3. Benabdelkader, A.; Draou, A.; AlKassem, A.; Toumi, T.; Denai, M.; Abdelkhalek, O.; Ben Slimene, M. Enhanced Power Quality in Single-Phase Grid-Connected Photovoltaic Systems: An Experimental Study. *Energies* **2023**, *16*, 4240. [CrossRef]
4. Steurer, M.; Frohlich, K. The impact of inrush currents on the mechanical stress of high voltage power transformer coils. *IEEE Trans. Power Deliv.* **2002**, *17*, 155–160. [CrossRef]
5. Mo, C.; Ji, T.Y.; Zhang, L.L.; Wu, Q.H. Equivalent statistics based inrush identification method for differential protection of power transforme. *Electr. Power Syst. Res.* **2022**, *203*, 107664. [CrossRef]
6. Sun, J.; Hu, K.; Fan, Y.; Liu, J.; Yan, S.; Zhang, Y. Modeling and Experimental Analysis of Overvoltage and Inrush Current Characteristics of the Electric Rail Traction Power Supply System. *Energies* **2022**, *15*, 9308. [CrossRef]
7. Samet, H.; Shadaei, M.; Tajdinian, M. Statistical discrimination index founded on rate of change of phase angle for immunization of transformer differential protection against inrush current. *Int. J. Electr. Power Energy Syst.* **2022**, *134*, 107381. [CrossRef]
8. Ruhan, Z.; Mansor, N.N.B.; Illias, H.A. Identification of Inrush Current Using a GSA-BP Network. *Energies* **2023**, *16*, 2340. [CrossRef]
9. Rane, M.; Wagh, S. Stability enhancement of transformered PV system using inrush mitigation techniques. In Proceedings of the 2017 North American Power Symposium (NAPS), Morgantown, WV, USA, 17–19 September 2017.
10. Xu, W.; Abdulsalam, S.G.; Cui, Y.; Liu, X. A sequential phase energization technique for transformer inrush current reduction—Part II: Theoretical analysis and design guide. *IEEE Trans. Power Deliv.* **2005**, *20*, 950–957. [CrossRef]
11. Seo, H.C.; Kim, C.H.; Rhee, S.B.; Kim, J.C.; Hyun, O.B. Superconducting Fault Current Limiter Application for Reduction of the Transformer Inrush Current: A Decision Scheme of the Optimal Insertion Resistance. *IEEE Trans. Appl. Supercond.* **2010**, *20*, 2255–2264. [CrossRef]
12. Madani, S.M.; Rostami, M.; Gharehpetian, G.B.; Maram, R.H. Improved bridge type inrush current limiter for primary grounded transformers. *Electr. Power Syst. Res.* **2013**, *95*, 1–8. [CrossRef]
13. Tseng, H.T.; Chen, J.F. Bidirectional impedance-type transformer inrush current limiter. *Electr. Power Syst. Res.* **2013**, *104*, 193–206. [CrossRef]
14. Ahmed, A.A.; Abdelsalam, H.A. Mitigation of transformer-energizing inrush current using grid-connected photovoltaic system. *Int. J. Electr. Power Energy Syst.* **2016**, *79*, 312–321. [CrossRef]
15. Guo, Y.; Zheng, Z.; Xie, Q.; Zhao, J. Study of Resistive Type SFCL for Limiting Inrush Current of LCC-HVDC Converter Transformer. *IEEE Trans. Appl. Supercond.* **2021**, *31*, 1–4. [CrossRef]
16. Wang, Y.; Yin, X.; Qiao, J.; Tan, L.; Xu, W. Inrush current suppression technology for floating nuclear power plants based on connecting Pre-T in series. *Int. J. Electr. Power Energy Syst.* **2022**, *135*, 107508. [CrossRef]
17. Molcrette, V.; Kotny, J.L.; Swan, J.P.; Brudny, J.F. Reduction of inrush current in a single-phase transformer using virtual air-gap technique. *IEEE Trans. Magn.* **1998**, *34*, 1192–1194. [CrossRef]
18. Cheng, C.K.; Chen, J.F.; Liang, T.J.; Chen, S.D. Transformer design with consideration of restrained inrush current. *Int. J. Electr. Power Energy Syst.* **2006**, *28*, 102–108. [CrossRef]
19. Farazmand, A.; De León, F.; Zhang, K.; Jazebi, S. Analysis, Modeling, and Simulation of the Phase-Hop Condition in Transformers: The Largest Inrush Currents. *IEEE Trans. Power Deliv.* **2014**, *29*, 1918–1926. [CrossRef]
20. Islam, M.M.; Muttaqi, K.M.; Sutanto, D. A Saturated Amorphous Alloy Core-Based Inrush Current Limiter to Eliminate Inrush Currents and Restrain Harmonics during Transformer Energization. *IEEE Trans. Ind. Appl.* **2021**, *57*, 6634–6645. [CrossRef]
21. Dogan, R.; Jazebi, S.; De León, F. Investigation of Transformer-Based Solutions for the Reduction of Inrush and Phase-Hop Currents. *IEEE Trans. Power Electron.* **2016**, *31*, 3506–3516. [CrossRef]

22. Kovan, B.; De Leon, F.; Czarkowski, D.; Zabar, Z.; Birenbaum, L. Mitigation of Inrush Currents in Network Transformers by Reducing the Residual Flux with an Ultra-Low-Frequency Power Source. *IEEE Trans. Power Deliv.* **2011**, *26*, 1563–1570. [CrossRef]
23. De León, F.; Farazmand, A.; Jazebi, S.; Deswal, D.; Levi, R. Elimination of Residual Flux in Transformers by the Application of an Alternating Polarity DC Voltage Source. *IEEE Trans. Power Deliv.* **2015**, *30*, 1727–1734. [CrossRef]
24. Sanati, S.; Alinejad-Beromi, Y. Fast and Complete Mitigation of Residual Flux in Current Transformers Suitable for Auto-Reclosing Schemes Using Jiles-Atherton Modeling. *IEEE Trans. Power Deliv.* **2022**, *37*, 765–774. [CrossRef]
25. Hajipour, E.; Salehizadeh, M.; Vakilian, M.; Sanaye-Pasand, M. Residual Flux Mitigation of Protective Current Transformers Used in an Autoreclosing Scheme. *IEEE Trans. Power Deliv.* **2016**, *31*, 1636–1644. [CrossRef]
26. Zhang, S.; Yao, C.; Zhao, X.; Li, J.; Liu, X.; Yu, L.; Ma, J.; Dong, S. Improved Flux-Controlled VFCV Strategy for Eliminating and Measuring the Residual Flux of Three-Phase Transformers. *IEEE Trans. Power Deliv.* **2020**, *35*, 1237–1248. [CrossRef]
27. Prikler, L.; Banfai, G.; Ban, G.; Becker, P. Reducing the magnetizing inrush current by means of controlled energization and de-energization of large power transformers. *Electr. Power Syst. Res.* **2006**, *76*, 642–649. [CrossRef]
28. Chiesa, N.; Høidalen, H.K. Novel Approach for Reducing Transformer Inrush Currents: Laboratory Measurements, Analytical Interpretation and Simulation Studies. *IEEE Trans. Power Deliv.* **2010**, *25*, 2609–2616. [CrossRef]
29. Parikh, U.; Bhalja, B.R. Mitigation of magnetic inrush current during controlled energization of coupled un-loaded power transformers in presence of residual flux without load side voltage measurements. *Int. J. Electr. Power Energy Syst.* **2016**, *76*, 156–164. [CrossRef]
30. Cano-González, R.; Bachiller-Soler, A.; Rosendo-Macías, J.A.; Álvarez-Cordero, G. Controlled switching strategies for transformer inrush current reduction: A comparative study. *Electr. Power Syst. Res.* **2017**, *145*, 12–18. [CrossRef]
31. Bejmert, D.; Kereit, M.; Boehme, K. Controlled energization procedures of power transformers. *Int. J. Electr. Power Energy Syst.* **2022**, *135*, 107555. [CrossRef]
32. Cavallera, D.; Oiring, V.; Coulomb, J.; Chadebec, O.; Caillault, B.; Zgainski, F. A New Method to Evaluate Residual Flux Thanks to Leakage Flux, Application to a Transformer. *IEEE Trans. Magn.* **2014**, *50*, 1005–1008. [CrossRef]
33. Wei, C.; Li, X.; Yang, M.; Ma, Z.; Hou, H. Novel Remanence Determination for Power Transformers Based on Magnetizing Inductance Measurements. *Energies* **2019**, *12*, 4616. [CrossRef]
34. Huo, C.; Wu, S.; Yang, Y.; Liu, C.; Wang, Y. Residual Flux Density Measurement Method of Single-Phase Transformer Core Based on Time Constant. *IEEE Access* **2020**, *8*, 171479–171488. [CrossRef]
35. Huo, C.; Wang, Y.; Zhao, Z.; Liu, C. Residual Flux Measurement of the Single-Phase Transformer Based on Transient Current Method. *IEEE Trans. Appl. Supercond.* **2020**, *30*, 1–5. [CrossRef]
36. Wu, S.; Ren, Y.; Wang, Y.; Huo, C.; Liu, C. Residual Flux Measurement of Power Transformer Based on Transient Current Difference. *IEEE Trans. Magn.* **2022**, *58*, 1–5. [CrossRef]
37. Huo, C.; Wang, Y.; Wu, S.; Yang, Y.; Zhao, Z. Residual Flux Density Measurement Method for Transformer Core Considering Relative Differential Permeability. *IEEE Trans. Magn.* **2021**, *57*, 1–4. [CrossRef]
38. Zhang, H.; Long, J.; Li, X.; Xu, Y.; Shi, J.; Ren, L.; Yang, W.; Wang, Z.; Chen, M. A New Method to Measure the Residual Flux by Magnetic Sensors and a Finite Element Model. *IEEE Trans. Instrum. Meas.* **2023**, *72*, 1–10. [CrossRef]
39. Vulin, D.; Milicevic, K.; Biondic, I.; Petrovic, G. Determining the Residual Magnetic Flux Value of a Single-Phase Transformer Using a Minor Hysteresis Loop. *IEEE Trans. Power Deliv.* **2021**, *36*, 2066–2074. [CrossRef]
40. Taylor, D.I.; Law, J.D.; Johnson, B.K.; Fischer, N. Single-Phase Transformer Inrush Current Reduction Using Prefluxing. *IEEE Trans. Power Deliv.* **2012**, *27*, 245–252. [CrossRef]
41. Zirka, S.E.; Moroz, Y.I.; Chiesa, N.; Harrison, R.G.; Høidalen, H.K. Implementation of Inverse Hysteresis Model Into EMTP—Part II: Dynamic Model. *IEEE Trans. Power Deliv.* **2015**, *30*, 2233–2241. [CrossRef]
42. Sima, W.; Peng, D.; Yang, M.; Liu, Y.; Duan, P.; Deng, J.; Qian, H. Low-frequency model for single-phase transformers based on the three-component Preisach model considering deep saturation. *Int. J. Electr. Power Energy Syst.* **2019**, *110*, 107–117. [CrossRef]
43. Zirka, S.E.; Moroz, Y.I.; Marketos, P.; Moses, A.J.; Jiles, D.C.; Matsuo, T. Generalization of the classical method for calculating dynamic hysteresis loops in grain-oriented electrical steels. *IEEE Trans. Magn.* **2008**, *44*, 2113–2126. [CrossRef]
44. Zirka, S.E.; Moroz, Y.I.; Harrison, R.G.; Chwastek, K. On physical aspects of the Jiles-Atherton hysteresis models. *J. Appl. Phys.* **2012**, *112*, 043916. [CrossRef]
45. Wang, Y.; Liu, Z. Estimation Model of Core Loss Under DC Bias. *IEEE Trans. Appl. Supercond.* **2016**, *26*, 1–5. [CrossRef]
46. Chiesa, N.; Avendaño, A.; Høidalen, H.K.; Mork, B.A.; Ishchenko, D.; Kunze, A.P. On the ringdown transient of transformers. In Proceedings of the International Conference on Power Systems Transients (IPST'07), Lyon, France, 4–7 June 2007.
47. Laithwaite, E.R. Magnetic equivalent circuits for electrical machines. *Proc. IET* **1967**, *114*, 1805–1809.
48. Justus, O. *Dynamisches Verhalten Elektrischer Maschinen: Eine Einführung in Die Numerische Modellierung mit PSPICE*; Vieweg: Wiesbaden, Germany, 1991; pp. 10–30.
49. Zirka, S.E.; Moroz, Y.I.; Arturi, C.M.; Chiesa, N.; Hoidalen, H.K. Topology-Correct Reversible Transformer Model. *IEEE Trans. Power Deliv.* **2012**, *27*, 2037–2045. [CrossRef]
50. Abdulsalam, S.G.; Xu, W.; Neves, W.L.A.; Liu, X. Estimation of transformer saturation characteristics from inrush current waveforms. *IEEE Trans. Power Deliv.* **2006**, *21*, 170–177. [CrossRef]
51. Bernard, Y.; Mendes, E.; Ren, Z. Determination of the distribution function of Preisach's model using centred cycles. *Compel Int. J. Comput. Math. Electr.* **2000**, *19*, 997–1006. [CrossRef]

52. Sima, W.; Zou, M.; Yang, M.; Peng, D.; Liu, Y. Saturable reactor hysteresis model based on Jiles–Atherton formulation for ferroresonance studies. *Int. J. Electr. Power Energy Syst.* **2018**, *101*, 482–490. [CrossRef]
53. Jiles, D.C. Frequency dependence of hysteresis curves in conducting magnetic materials. *J. Appl. Phys.* **1994**, *76*, 5849–5855. [CrossRef]
54. Mikhak-Beyranvand, M.; Faiz, J.; Rezaei-Zare, A.; Rezaeealam, B. Electromagnetic and thermal behavior of a single-phase transformer during Ferroresonance considering hysteresis model of core. *Int. J. Electr. Power Energy Syst.* **2020**, *121*, 106078. [CrossRef]
55. Podbereznaya, I.; Pavlenko, A. Accounting for dynamic losses in the Jiles-Atherton model of magnetic hysteresis. *J. Magn. Magn. Mater.* **2020**, *513*, 167070. [CrossRef]
56. Mayergoyz, I.D.; Friedman, G. Generalized Preisach model of hysteresis. *IEEE Trans. Magn.* **1988**, *24*, 212–217. [CrossRef]
57. Preisach, F. Über die magnetischeNachwirkung. *Z. Phys.* **1935**, *94*, 277–302. [CrossRef]
58. Lu, M.; Leonard, P.J.; Marketos, P.; Meydan, T.; Moses, A.J. Dependence of dynamic Preisach distribution function on magnetizing frequencies. *IEEE Trans. Magn.* **2006**, *42*, 951–954. [CrossRef]

Disclaimer/Publisher's Note: The statements, opinions and data contained in all publications are solely those of the individual author(s) and contributor(s) and not of MDPI and/or the editor(s). MDPI and/or the editor(s) disclaim responsibility for any injury to people or property resulting from any ideas, methods, instructions or products referred to in the content.